

ADVANCED MATERIALS

Supporting Information

for *Adv. Mater.*, DOI: 10.1002/adma.201908258

Color-Selective Printed Organic Photodiodes for Filterless Multichannel Visible Light Communication

*Noah Strobel, Nikolaos Droseros, Wolfgang Köntges,
Mervin Seiberlich, Manuel Pietsch, Stefan Schlisske, Felix
Lindheimer, Rasmus R. Schröder, Uli Lemmer, Martin
Pfannmöller, Natalie Banerji, and Gerardo Hernandez-Sosa**

Supporting Information**Color-selective Printed Organic Photodiodes for Filterless Multichannel Visible Light Communication**

Noah Strobel, Nikolaos Droseros, Wolfgang Köntges, Mervin Seiberlich, Manuel Pietsch,
 Stefan Schlisske, Felix Lindheimer, Rasmus R. Schröder, Uli Lemmer, Martin Pfannmöller,
 Natalie Banerji, Gerardo Hernandez-Sosa*

State-of-the-art Performance Comparison

Table S1: Comparison of various color selective OPDs fabricated from solution. Different material classes and approaches are included and compared to our devices.

| | Material | Approach | Wavelength [nm] | Peak SR [mA cm ⁻²] | Cut-off [kHz] | year | Ref. |
|------------------------|---------------------------|----------------------|-----------------|--------------------------------|---------------|-----------|------|
| Blue & green selective | Dendrimer + Fullerene | selective absorption | 350-600 | 82 | - | 2014 | [1] |
| | Perovskite single crystal | CCN | 550-600 | 14 | 1.6 | 2015 | [2] |
| | squarylium | Selective absorption | 450-700 | 314 | - | 2017 | [3] |
| | Polymer only | Selective absorption | 300-500 | 16 | 10.6 | 2016 | [4] |
| | PIF:IDFBR | Selective absorption | 400-600 | 73 | 3500 | This work | |
| Red selective | perovskite | CCN + Dye | 600-700 | 63 | 297 | 2015 | [5] |
| | Polymer + Fullerene | Cavity | 650-750 | 200 | 1000 | 2017 | [6] |
| | Polymer + Fullerene | Filter | 500-750 | 183 | 1.1 | 2018 | [7] |
| | Polymer +Fullerene | CCN + Cavity | 600-650 | 126 | 100 | 2019 | [8] |

| PIF:ITIC-4F | Selective Absorption | 550-800 | 229 | 1500 | This work |
|-----------------------------------|----------------------|---------|-----|------|-----------|
| CCN = Charge Collection Narrowing | | | | | |

Printing Process Development

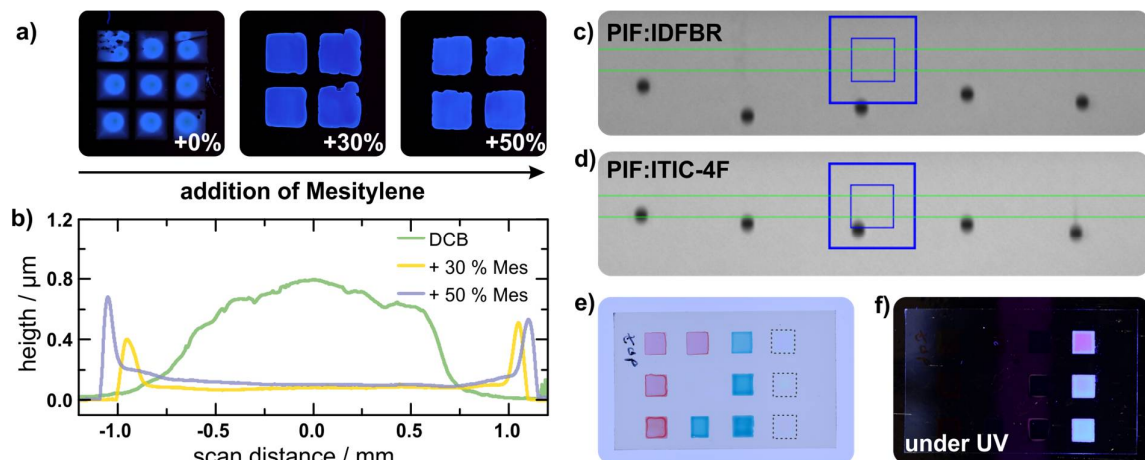
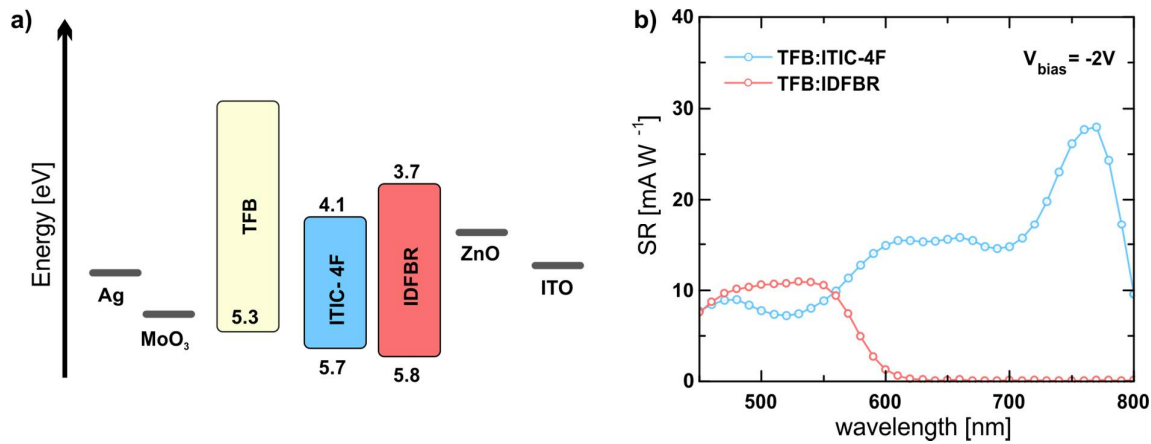


Figure S1 a) Photographs of printed squares from a pristine PIF ink of 20 g L^{-1} in dichlorobenzene with increasing addition of Mesitylene. b) Height profiles of the printed layers. c) Droplets ejected from the inkjet printhead of the blue selective PIF:IDFBR and d) of the red selective PIF:ITIC-4F ink. The exact same printing parameters are used. e) Squares printed with PIF:IDFBR (red) PIF:ITIC-4F (blue) and pristine PIF (transparent, marked by dotted line). The printing resolution is increased from top to bottom. f) The same squares under UV illumination.

The development of the printing process for the active layer was carried out with a pristine PIF solution in dichlorobenzene (DCB). As is visible in Figure S1a and b, the single solvent ink shows inhomogeneous drying effects, which lead to a transfer of the material to the center of the printed structure. By addition of mesitylene as a second solvent, the drying is considerably improved allowing for homogeneous flat layers. At the edge of the pattern a small coffee ring forms, which lies outside of the active area and can therefore be neglected for the successful device operation. The NFAs are then added to the developed PIF ink. Due to the invariance of the viscoelastic properties, the same printing parameters (waveform, dropspacing, temperature etc.) were transferable. Figure S1c and d depict the ejected droplets of the PIF:NFA inks with these printing settings showing the same droplet quality. Printed layers from the various inks are shown in Figure S1e and f under ambient and UV-illumination, respectively. The same drying behavior is observed for the various inks even

with different printing resolution settings leading to layers of various thicknesses. Under UV light, the PIF layers show photoluminescence whereas in the BHJ layers luminescence is quenched due to the successful exciton separation.



Color selective OPDs based on TFB

Figure S2 a) Energy level diagram of devices containing TFB:NFA blends as the photoactive layer. b) Spectral responsivity of the respective devices.

The demonstrated concept of combining a transparent polymer donor with selective NFAs can also be applied to other material combinations. Figure S2 displays the combination of TFB with IDFBR and ITIC-4F, respectively for color selective OPDs. For this set of devices, the layers were spincoated. The energy levels are sufficiently aligned to allow for exciton separation and transport to the respective electrodes. The spectral responsivity of the devices is governed by the absorption range of the NFAs. As for PIF, TFB does not affect the responsivity of the device in the visible range but controls the viscoelastic properties of the ink.

Further Details on ATEM measurements

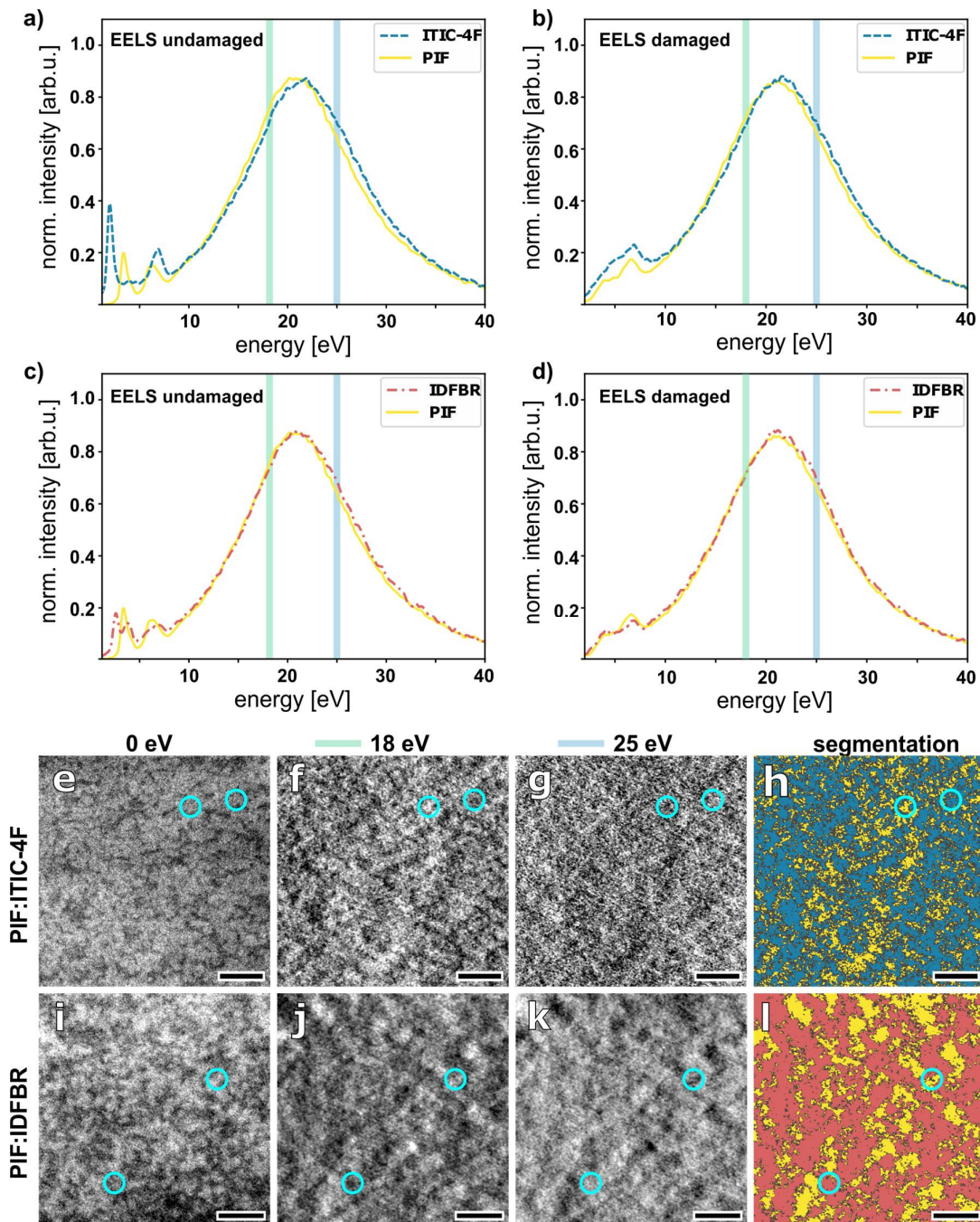
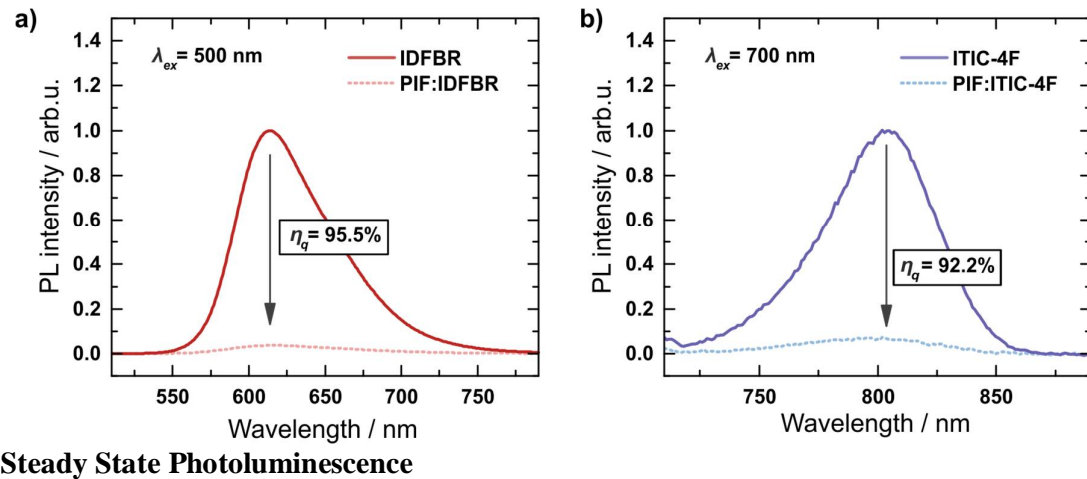


Figure S3 TEM/ATAM analysis of PIF:ITIC-4F and PIF:IDFBR blends. **a)** Spectra of pristine PIF and ITIC-4F acquired by electron energy-loss spectroscopy (EELS). **b)** Spectra at the same sample position as in (a) after an electron dose of 1.5×10^5 electrons per nm^2 . **c)** and **d)** show the EEL spectra of PIF and IDFBR before and after presumed damage by the

increased total electron dose. Note that the signature for damage is confined to the low energy loss region, indicating damage mainly to the long range conjugated electronic structures. The more persistent signal at larger energy loss most likely represents the core structure of molecules, which withstand larger electron dose and are then used as readout for segmentation, i.e. they still represent the distribution of materials and thus device morphology. The colored bands at energy-loss values of 18 eV and 25 eV indicate the energies for the inelastic images in the second and third column (*f,j* and *g,k*) acquired by electron spectroscopic imaging (ESI). *e-l*) Zero-loss bright-field TEM images (first column; *e,i*), ESI images (second and third column) and material distribution maps (fourth column; *h,l*). Scale bars represent 100 nm. Circles mark regions corresponding to donor and acceptor phases, showing inverted contrast in the inelastic images but similar signal in the bright-field TEM image in the first column. Hence, the contrast in the ESI images cannot arise from thickness and density variations, i.e. mass-density differences, but indicates different material phases. Supplementary Figure S3a-d shows the electron energy-loss (EEL) spectra for the pristine materials. We observe small differences between PIF and the respective NFA in the broad feature ranging from 10 eV to 40 eV corresponding to plasmons localized on individual molecules. This difference is stable despite the initial damage induced by the electron beam on the organic layers which is observed in low energy range <10 eV of the normalized EEL spectra. Through electron spectroscopic imaging (ESI) the different material phases are identified by differences in images recorded at the different energies in the range of the plasmon excitation. Preceding to data analysis, the recorded inelastic images were aligned by affine image registration. The ESI series were normalized by the sum of all inelastic images in the series to remove any remaining mass-density contrast in the images, which otherwise might conceal the material. For noise reduction of the normalized ESI series principal component analysis was applied using Hyperspy.^[9] Using ilastik, an open source software for image classification and segmentation based on statistical analysis and supervised machine learning^[10], the ESI spectra were classified into distinct classes. The details of this analysis

are described elsewhere.^[11] Thickness measurements were performed by the Fourier-log-method in the TEM.^[12]



Steady State Photoluminescence

Figure S4 a) PL spectra of pristine IDFBR and the PIF:IDFBR blend upon excitation at 500 nm

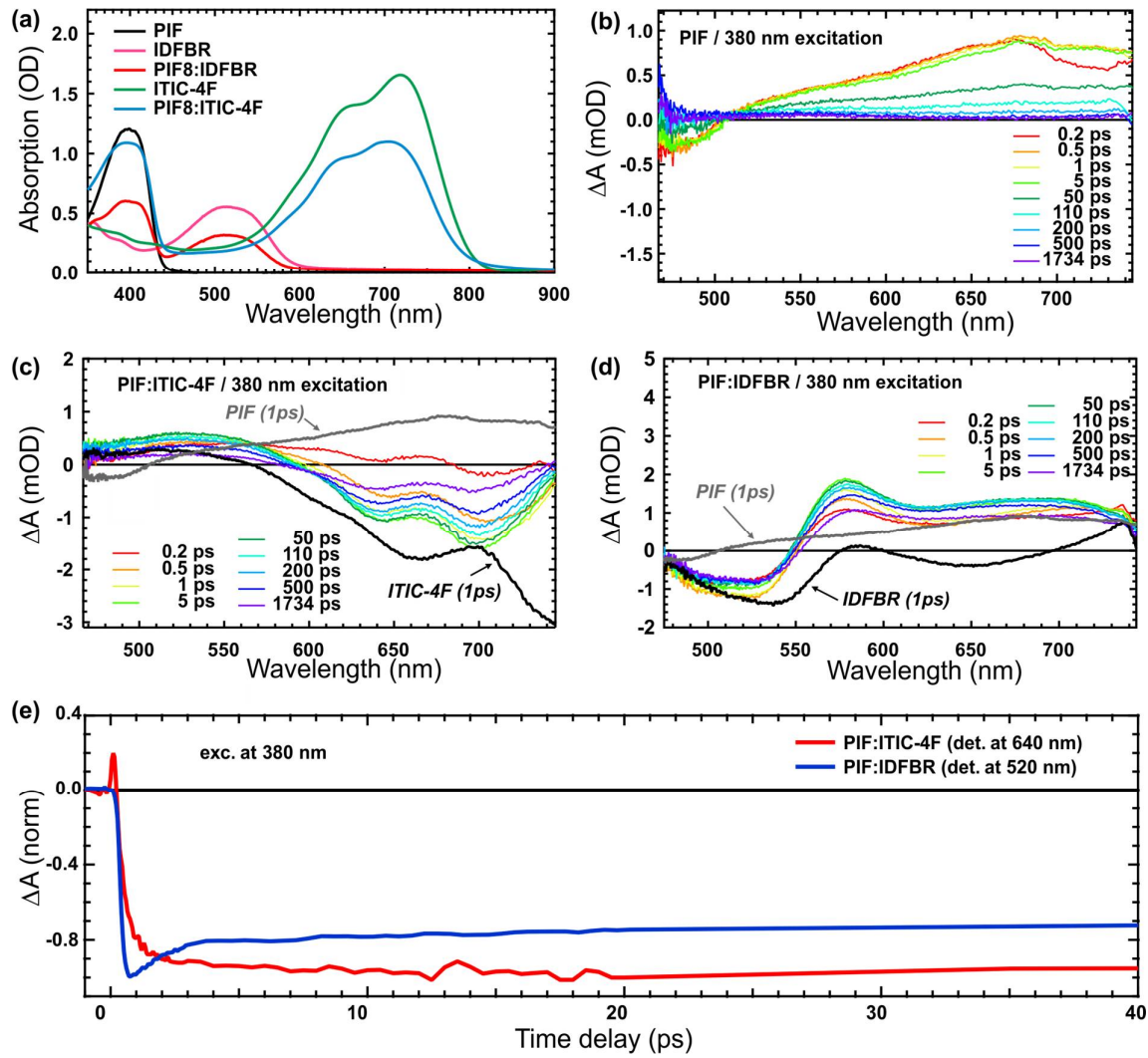
b) PL spectra of pristine ITIC-4F and the PIF:ITIC-4F blend upon excitation at 700 nm

To confirm the successful separation of exciton generated in the NFAs, steady state

photoluminescence (PL) measurements were performed on pristine NFA samples as well as

on blends with PIF. The Measurements show a strong quenching of the PL upon addition of

the PIF to the NFA suggesting an efficient exciton splitting at the donor-acceptor interface.

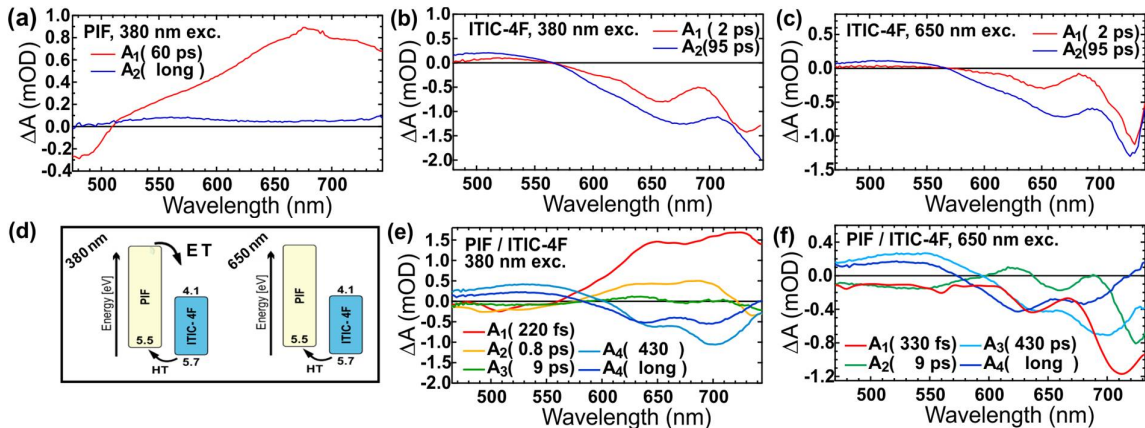


Electron Transfer probed by TA

Figure S5: a) Steady state absorption spectra of all the samples. TA spectra recorded at different time delays after excitation at 380 nm for b) neat PIF, c) PIF:ITIC-4F and d) PIF:IDFBR. The TA spectra of the neat acceptor and donor films at 1 ps are shown for comparison. e) Dynamics probed in the GSB of the acceptors (640 nm for PIF:ITIC-4F and 520 nm for PIF:IDFBR). The observed ultrafast rise is caused by electron transfer from photoexcited PIF to the NFAs (which is mixed with some intrinsic hole transfer on the < 1 ps time scale).

In the main manuscript we have examined only the case where the NFA is selectively excited, leading to hole transfer in the blends. When the blends are excited in a spectral region where

also the PIF donor absorbs (at 380 nm), electron transfer from PIF to the NFA is expected (Figure S5). The early (0.2 ps) TA spectra of both blends with 380 nm excitation are clearly distinct from the ones of the neat acceptor and donor, but already contain the signatures of photo-generated charges that remain at long time delays. This shows that prompt electron transfer (within the 60 fs time resolution of the experiment) occurs in both cases. Such ultrafast electron transfer is typical in OPV blends, especially with high driving forces as are present here (> 1 eV, Figure 2a). A further rise of the acceptor GSB evidences some diffusion-mediated delayed electron transfer, which occurs within a picosecond in both blends. Weak spectral changes that then occur on an even slower time scale with 380 nm excitation are due to hole transfer caused by residual excitation of the acceptors. Because of the occurrence of both electron transfer and hole transfer at this excitation wavelength, the dynamics are more complex, but could be disentangled using global analysis (Figures S6 and S7).



Global analysis results of TA on PIF:ITIC-4F

Figure S6: Decay-associated spectra (DAS) obtained by multi-exponential global analysis of the TA dynamics at all probe wavelengths for a) neat PIF film under 380 nm excitation. b) and c) DAS of neat ITIC-4F film under 380 nm and 650 nm excitation. d) Electron and hole transfer processes that take place in the blend under the two excitation wavelengths. e) and f) DAS for the PIF:ITIC-4F blend under 380 nm and 650 nm excitation.

Figure S6 shows multi-exponential global analysis of the dynamics probed by TA. In the pristine PIF a 60 ps component due to exciton recombination and an offset due to long-lived species (charges or triplet states) are observed for excitation at 380 nm. The pristine ITIC-4F shows a bi-phasic exciton decay with time constants of 2 ps and 95 ps for 380 nm as well as for 650 nm excitation. In the case of the blend at 380 nm excitation various components are observed. A 220 fs component that is mainly due to electron transfer (showing a clear rise of the acceptor GSB and rise of the charge PIA), a 0.8 ps component that can be assigned to a mixture of electron transfer and hole transfer (rise of the acceptor GSB, decay of the acceptor stimulated emission and rise of the charge PIA), a weak 9 ps component due to hole transfer (decay of the acceptor stimulated emission and rise of the charge PIA), a 430 ps component which is attributed to geminate recombination of charges, and the offset (long component) due to long-lived charges. With 650 nm selective excitation of the acceptor, the 0.3 ps and

9 ps components are caused by hole transfer, while the 430 ps and long components are due to geminate recombination and long-lived charges.

Global analysis results of TA on PIF:IDFBR

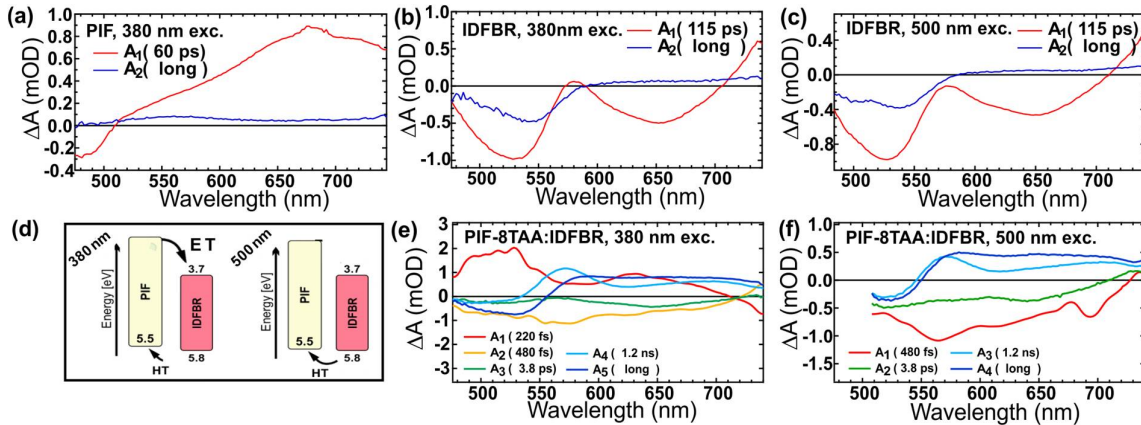
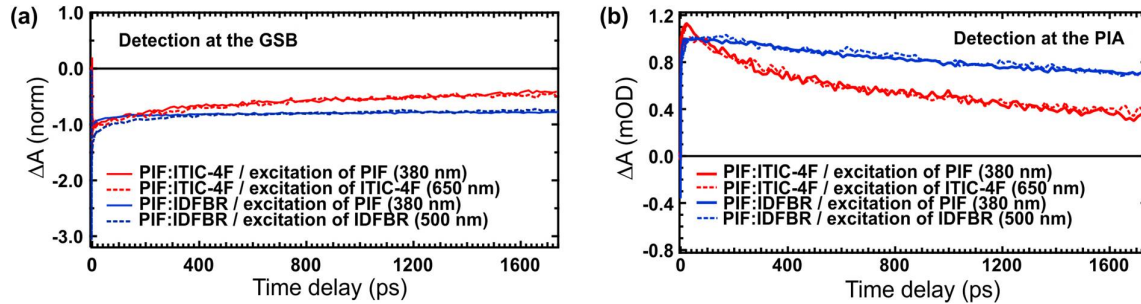


Figure S7: Decay-associated spectra (DAS) obtained by multi-exponential global analysis of the TA dynamics at all probe wavelengths for a) neat PIF film under 380 nm excitation. b) and c) DAS of neat IDFBR film under 380 nm and 500 nm excitation. In both cases, exciton decay occurs with a time constant of 115 ps and there is a long-lived component (without any stimulated emission signature) possibly due to charges or the triplet state. d) Electron and hole transfer processes that take place in the blend under the two excitation wavelengths. e) and f) DAS for the PIF:IDFBR blend under 380 nm and 500 nm excitation.

Figure S7 depicts the Global analysis of the PIF:IDFBR system. The pristine PIF has been discussed above. The pristine IDFBR shows at 380 nm and 500 nm an exciton decay that occurs with a time constant of 115 ps and there is a long-lived component (without any stimulated emission signature) possibly due to charges or the triplet state. Similarly, to the case of the ITIC-4F, multiple components are present in the blends. With 380 nm excitation, the 0.2 ps component is mainly due to electron transfer (leading to a rise of the acceptor GSB), the 0.5 ps and 3.8 ps components are assigned to hole transfer, the 1200 ps component is attributed to geminate recombination of charges, and the offset (long component) to long-lived charges. With 650 nm selective excitation of the acceptor, the 0.5 ps and 3.8 ps

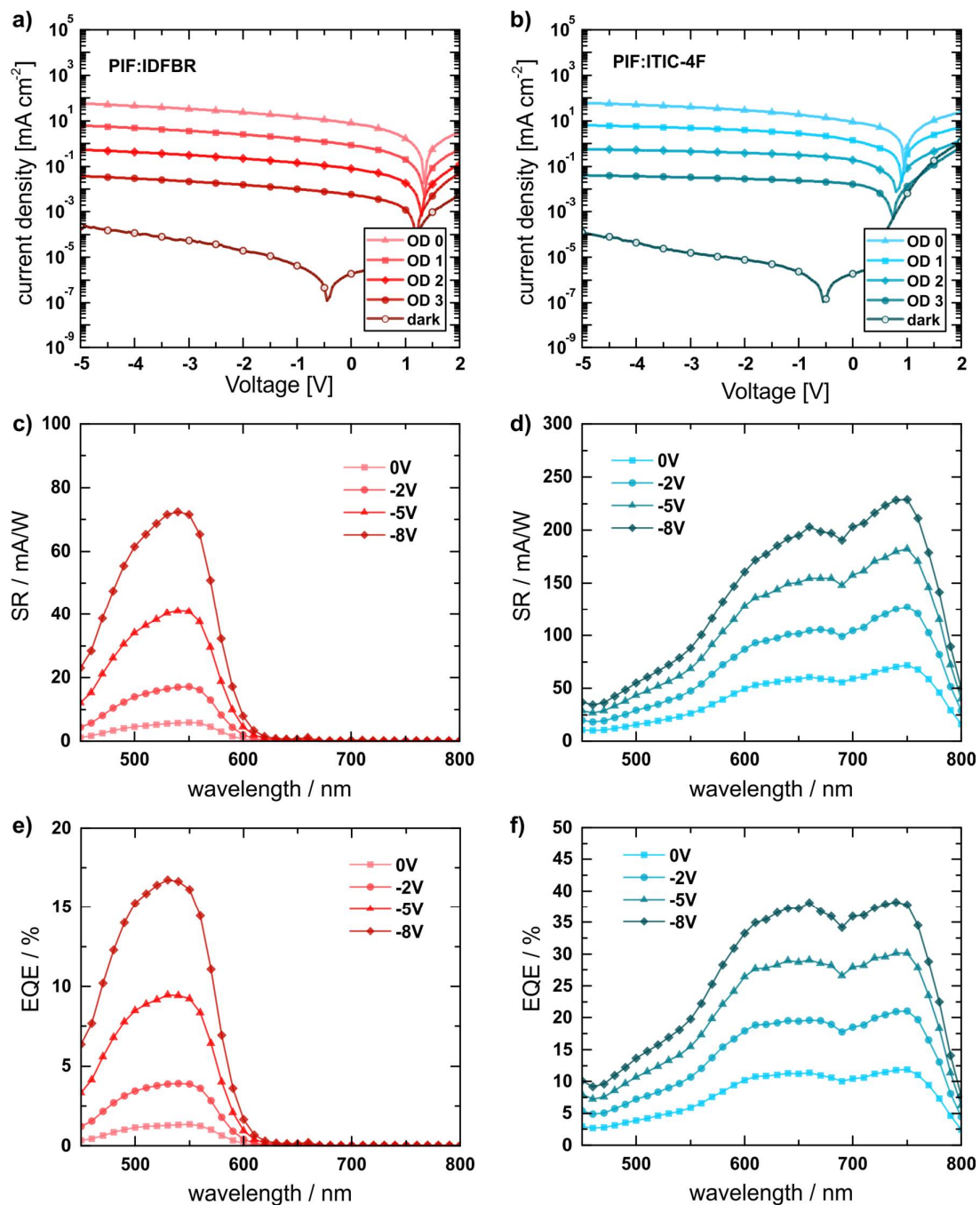
components are caused by hole transfer, while the 1200 ps and long components are due to geminate recombination and long-lived charges.



Recombination at long times:

Figure S8: TA dynamics of the PIF:ITIC-4F (red) and the PIF:IDFBR (blue) detected (a) at the acceptor GSB of each blend and (b) in the PIA band. Continuous lines show the dynamics with excitation of both the donor and the acceptor at 380 nm while dashed lines show the dynamics with excitation of the acceptor.

When looking at the long time delays (> 200 ps), the TA spectra of the two systems no longer significantly change shape (since the charge transfer processes are complete), but there is an overall decay of their signatures due to geminate recombination. Comparing the dynamics of the GSB and PIA at long time delays (Figure S8), we see that the recombination is slightly more pronounced in PIF:ITIC-4F, but does not depend on the excitation wavelength. Both blends show nevertheless a significant offset due to long-lived charges.



Additional Steady State Characteristics

Figure S9: Current-voltage characteristics with different illumination intensities for printed a) PIF:IDFBR and b) PIF:ITIC-4F devices. Intensities are varied by inserting optical density filters (OD) to reduce the initial optical power of 12 mW corresponding to OD 0. c) and d)

Spectral responsivity of the printed devices at different reverse bias voltages. e) and f) EQE Spectra of the printed devices at the different reverse bias voltages.

Figure S9 displays additional steady state device characteristics including JV-curves at different light intensities. The dark current curves experience a slight hysteresis which offsets the open circuit transition from negative to positive currents from 0 V to around -0.5 V. This hysteresis can be attributed to trapping and de-trapping of deep trapped charges.^[13,14] The hysteresis has no effect outside the voltage range of 1 V or for currents above 10 mA cm⁻². The linear increase of the current with intensity holds true for the entire measured reverse bias range. Additionally, high open circuit voltages are evident in the forward bias regime, surpassing 1 V for the PIF>IDFBR devices. This is related to the high HOMO-LUMO difference between donor and NFA. Figures S9c,d and e,f show the spectral responsivities and EQE spectra at different reverse bias voltages for inkjet-printed and spin coated reference devices, demonstrating the similar device performance of the inkjet-printed OPDs.

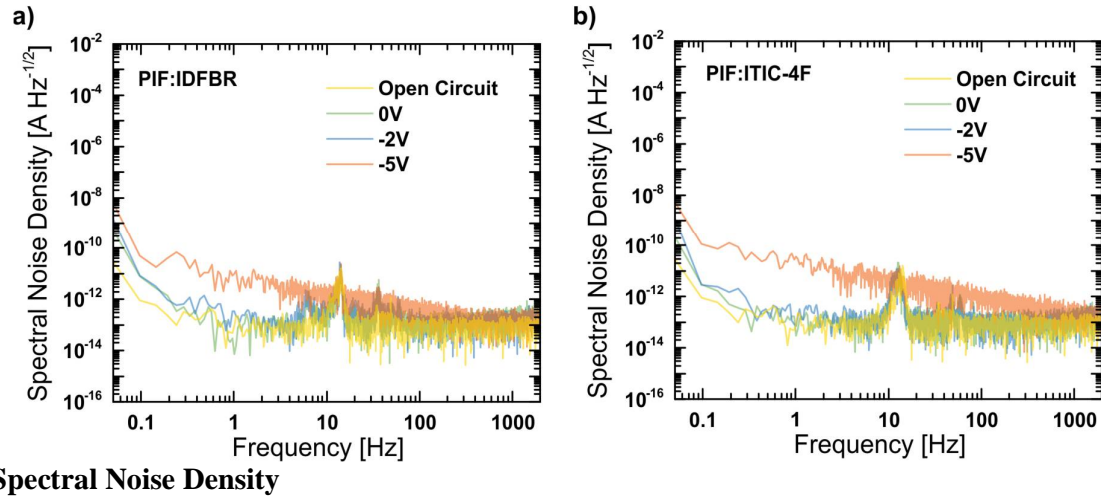
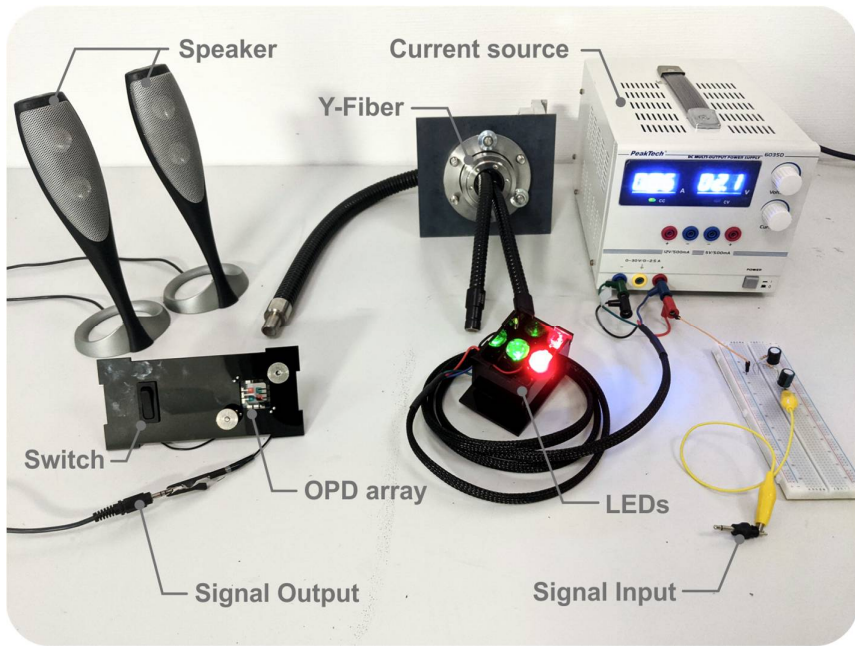


Figure S10: Spectral noise densities of a) printed PIF:IDFBR and b) PIF:ITIC-4F devices at different reverse bias voltages. For comparison the measured noise density measured for open circuit is plotted as well.

The noise spectral densities of PIF:IDFBR and PIF:ITIC-4F devices are displayed in Figure S10 together with the spectrum of the measurement system at open circuit. The similarity in the noise spectra for open circuit, 0 V and -2 V indicates that the detection limit of the setup is reached. The actual noise of the devices at the respective voltages is therefore expected to be lower leading to an underestimation of the specific detectivity. For -5 V the noise increases above the detection limit for the low frequency regime. However, above 1 kHz it reaches the limit again suggesting, that even for -5 V the white noise regime lies below the detection limit. Based on the noise spectral density S_{noise} the specific detectivity D^* is calculated from the spectral responsivity SR and the area A with the following equation:

$$D^* = \frac{SR\sqrt{A}}{S_{noise}}$$



VLC system parts

Figure S11: Main parts used to realize the VLC system. Cables and wires connecting the different parts are removed to ensure better visibility.

References

- [1] A. K. Pandey, K. D. Johnstone, P. L. Burn, I. D. W. Samuel, *Sensors Actuators, B Chem.* **2014**, *196*, 245.
- [2] Y. Fang, Q. Dong, Y. Shao, Y. Yuan, J. Huang, *Nat. Photonics* **2015**, *9*, 679.
- [3] W. Li, H. Guo, Z. Wang, G. Dong, *J. Phys. Chem. C* **2017**, *121*, 15333.
- [4] S. Yoon, J. Ha, J. Cho, D. S. Chung, *Adv. Opt. Mater.* **2016**, *4*, 1933.
- [5] Q. Lin, A. Armin, P. L. Burn, P. Meredith, **2015**, DOI 10.1038/NPHOTON.2015.175.
- [6] S. Ullrich, B. Siegmund, A. Mischok, A. Hofacker, J. Benduhn, D. Spoltore, K. Vandewal, **n.d.**, DOI 10.1021/acs.jpcllett.7b02571.
- [7] I. Deckman, P. B. Lechêne, A. Pierre, A. C. Arias, *Org. Electron.* **2018**, *56*, 139.
- [8] A. Yazmaciyan, P. Meredith, A. Armin, *Adv. Opt. Mater.* **2019**, 1801543.
- [9] F. de la Peña, E. Prestat, V. T. Fauske, P. Burdet, P. Jokubauskas, M. Nord, T. Ostasevicius, K. E. MacArthur, M. Sarahan, D. N. Johnstone, J. Taillon, J. Lähnemann, V. Migunov, A. Eljarrat, J. Caron, T. Aarholt, S. Mazzucco, M. Walls, T. Slater, F. Winkler, B. Martineau, G. Donval, R. McLeod, E. R. Hoglund, I. Alxneit, D. Lundeby, T. Henninen, L. F. Zagonel, A. Garmannslund, **2019**, DOI 10.5281/zenodo.3396791.
- [10] C. Sommer, C. Straehle, U. Kothe, F. A. Hamprecht, in *Proc. - Int. Symp. Biomed. Imaging*, **2011**, pp. 230–233.
- [11] M. Pfannmöller, H. Flügge, G. Benner, I. Wacker, C. Sommer, M. Hanselmann, S. Schmale, H. Schmidt, F. A. Hamprecht, T. Rabe, W. Kowalsky, R. R. Schröder, *Nano Lett.* **2011**, *11*, 3099.
- [12] R. F. Egerton, *Electron Energy-Loss Spectroscopy in the Electron Microscope*, Springer US, **2011**.
- [13] W. Brütting, H. Riel, T. Beierlein, W. Riess, *J. Appl. Phys.* **2001**, *89*, 1704.
- [14] Y.-J. Lin, *J. Appl. Phys* **2008**, *103*, 1.